

# On the Formation of Macroseggregations in Steel Ingot Castings

Menghuai Wu<sup>1</sup>, Laszlo Könözy<sup>1</sup>, Andreas Ludwig<sup>1</sup>, Wolfgang Schützenhöfer<sup>2</sup>, Robert Tanzer<sup>2</sup>

<sup>1</sup>Christian Doppler Laboratory for Multiphase Modeling of Metallurgical Processes, Dept. Metallurgy, Univ. Leoben, A-8700, Austria. <sup>2</sup>Böhler Edelstahl GmbH & Co KG, A-8605 Kapfenberg, Austria. menghuai.wu@mu-leoben.at

**Abstract.** A multiphase approach is used to study macrosegregation phenomena that occur during solidification of steel ingot castings. The goal is to enhance the understanding of different mechanisms of macrosegregation formation. 4 different cases are presented consecutively with increasing complexity of the model assumptions and increasing dimensions: (1) feeding-induced macroseggregations in 1-dimensional unidirectional solidification situation, (2) macroseggregations caused by thermosolutal buoyancy driven flow in a 2-dimensional axis symmetrical benchmark ingot, (3) macroseggregations caused by grain sedimentation in the same 2-dimensional ingot, and (4) macroseggregations which form during mixed equiaxed-columnar solidification in a full 3-dimensional benchmark ingot.

**Keywords:** macrosegregation, steel ingot, feeding flow, convection, sedimentation, CET (columnar-to-equiaxed transition).

## Introduction

It is understood that macroseggregations occur due to a relative motion between the liquid and solid phase during solidification. This relative motion can arise as a result of thermosolutal convection, shrinkage-induced feeding flow, flotation and sedimentation of free moving grains, mechanical or electromagnetic stirring, flow induced by pore or gas bubble formation, deformation of the solid skeleton, and capillary (Marangoni) force induced flow [1-6]. Because of the complexity of the coupled flow mechanisms and their multiphase nature, some macrosegregation phenomena, which are observed in the industry processes, are still quite difficult to predict quantitatively. As summarized by Beckermann: ‘while some successes have been reported in predicting measured macrosegregation patterns in industrially relevant casting processes, there are still numerous areas where further development is required [2].’ The current report is focused on the authors’ recent contributions to this topic. As such, a computational multi-fluid dynamics (CMFD) approach was used to study the formations of macroseggregations in the following 4 cases:

- (1) Macrosegregation caused by feeding flow during unidirectional solidification: This case was once studied by Flemings et al. with his classical LSRE (local solute redistribution equation) model [7-9].
- (2) Macroseggregations caused by thermosolutal buoyancy driven flow: A 2D axis symmetrical benchmark ingot casting is supposed to solidify with only columnar dendritic morphology.
- (3) Macroseggregations caused by grain sedimentation: The same 2D benchmark ingot casting as in case (2) is calculated, but now it is supposed to solidify with only globular equiaxed morphology.
- (4) Macroseggregations caused by thermo-solutal convection and grain sedimentation revealing mixed equiaxed-columnar morphology: The competitive crystal growth, the interaction between the columnar and equiaxed phases, and the columnar-to-equiaxed transition (CET) are considered.

For these investigations a general 3-phase mixed columnar-equiaxed solidification model, which was developed

by the authors [10-12], is used. A binary Fe-C alloy with initial concentration of 0.34 wt. % C is chosen. A simplified solidification path is employed as a single primary solid phase in either columnar or globular equiaxed morphology is assumed to form. Thus, there is no distinction between ferrite and austenite phases. Additional details relevant to the numerical model and thermophysical and thermodynamic data are described in previous publications [10-12].

## Case 1: Feeding flow-induced macrosegregation

A benchmark of a 1-D unidirectional solidification, as shown in Figure 1, was studied by Flemings et al. [7] and Kato et al. [9]. According to Flemings’ LSRE model,

$$\frac{\partial f_\ell}{\partial c_\ell} = -\frac{(1-\beta)}{(1-k)} \left( 1 - \frac{\bar{u}_\ell}{\bar{v}_\ell} \right) f_\ell = 0, \quad (1)$$

a typical concentration profile along the 1D benchmark reveals a positive segregation region in the vicinity of the wall (i.e. inverse segregation), a ‘steady state’ region in the mid-section of the sample, and a negative segregation region in the solidifying mushy zone. For the case of Figure 1, represented by unidirectional solidification against a cold mould wall where finite resistance to heat transfer exists at the interface, the extension of the width of the solidifying mushy zone with the time would lead to a positive segregation in the ‘steady state’ mid-section region [7]. All the symbols of the equation are defined in the Nomenclature. Flemings’ LSRE is often used to validate later numerical models [13]. Therefore, also we have tested our multiphase model against the LSRE model.

The bases of the current multiphase model and the Flemings’ LSRE model are the same: solute partitioning and redistribution in the mushy zone, and the mass/species conservation and transport with the flow through the mushy zone. For the same assumptions as the once Flemings’ used, the current multiphase conservation equations give Flemings’ LSRE (see Appendix A). Here we modify the general 3-phase mixed columnar-equiaxed solidifica-

tion model [10-12] with further model simplifications and process conditions:

- Mould filling is ignored. The casting starts to solidify from an initial temperature of 1785 K;
- Only two phases are considered: melt and columnar dendrite trunks. We suppose that there are no equiaxed grains nucleating in the calculation domain;
- Columnar dendrite morphology is approximated by step-wise growing cylinders with constant primary arm spacing;
- Columnar trunks grow from the mould wall. The position of the growing columnar tip front is tracked explicitly [10];
- Solidification shrinkage is the only mechanism to induce flow. Solid and liquid densities are:  $\rho_\ell = 7027 \text{ kg}\cdot\text{m}^{-3}$ ,  $\rho_s = 7321 \text{ kg}\cdot\text{m}^{-3}$ , respectively.
- A constant heat transfer coefficient of  $700 \text{ W}\cdot\text{m}^{-2}\cdot\text{K}^{-1}$  and a constant mould temperature of 300 K are applied on the mould boundary, and a ‘pressure inlet’ condition with constant temperature of 1785 K is applied on the open boundary.

As shown in Figure 2a, the simulation results show typical unidirectional solidification from a cold mould. The 1-D numerical results (Figure 2b) show maximum positive segregation (inverse segregation) at the mould surface, slightly positive segregation along the sample, and negative segregation at the end of the sample. Negative segregation occurs at the end of solidification, when feeding is insufficient. These results agree with Flemings’ analytical solution, and other experimental and numerical findings [7, 9, 13]. Figure 2b shows  $c_{\text{mix}}$ , the local mean concentration of solute, along the sample at three instants in time. Each curve shows the inverse segregated region at the wall, followed by a region of negative segregation within the mushy zone. This negative segregation corresponds to the region behind the columnar tip front where  $c_{\text{mix}}$  is always lower than  $c_0$ . This pattern of positive and negative segregation is caused only by feeding flow due to solidification shrinkage. The solute-rich melt in the mushy region is transported to the root of the dendrite trunks to feed the solidification shrinkage, while the space of the leaving interdendritic melt near the columnar tips has to be replaced by fresh melt ( $c_\ell = c_0$ ) from the bulk in front of the columnar tips.

## Case 2: Thermosolutal convection-induced macrosegregation

A small steel ingot benchmark (Figure 3) is simulated. Again, a two-phase columnar solidification model is used to study the formation of macrosegregations caused by thermosolutal convection only. The model simplifications and process conditions are summarized as follows:

- Mould filling is ignored, solidification starts with an initial concentration Fe-0.34 wt. % C and an initial temperature of 1785 K;
- Two phases are considered: the melt and columnar dendrite trunks. We suppose that there are no equiaxed grains nucleating in the calculation domain;

- The columnar dendrite morphology is approximated by step-wise growing cylinders with constant (primary arm) spacing;
- Those columnar trunks start to grow from side and bottom walls, whereby the columnar tip front is tracked explicitly;
- Solidification shrinkage is not considered, a Boussinesq approximation is used to treat thermosolutal convection. The thermal and solutal expansion coefficients of the melt are  $\beta_T = 2 \cdot 10^{-4} \text{ K}^{-1}$ ,  $\beta_c = 0.011 \text{ wt.\%}^{-1}$ , respectively;
- Constant heat transfer coefficients and constant mould and air temperatures are used (Figure 3);
- 2D axis symmetric calculations are carried out.

The final macrosegregation pattern predicted for the ingot is shown in Figure 4e: a small region with negative macrosegregation ( $c_{\text{mix}} < c_0$ ) is found in the upper surface region, particularly in the upper corners where  $c_{\text{mix}} \sim 0.33$ . In the lower corners a positive macrosegregation is predicted  $c_{\text{mix}} \sim 0.36$ . A large area of positive macrosegregation with  $c_{\text{mix}}$  up to 0.38 is located in the casting centre.

The solidification sequences and evolution of  $c_{\text{mix}}$  are shown in Figure 4a-d. The columnar tip front and volume fraction of the columnar phase ( $f_c$ -isolines) move from the outer region towards the bulk melt region. Due to thermosolutal convection, the ‘hot spot’ in the ingot centre moves upwards and is finally located slightly above the geometrical centre of the casting. During solidification an axis symmetric convection pattern develops. The melt near the mould wall has a higher density due to its lower temperature, and thus sinks downwards, while the hotter melt in the centre rises. One may argue that the solute-enriched, lower density interdendritic melt might rise and thus partially compensate or reverse the above mentioned convection pattern. However, with the given temperature gradient, the thermal buoyancy dominates over the solutal buoyancy. The downward flow near the columnar tip region and the upward flow in the bulk melt are the primary phenomena which lead to the final macrosegregation.

The mechanisms which lead to the formation of macrosegregations in the corner regions are analysed as follows. With the assumption of stationary solid and no solidification shrinkage, seeing Appendix B, the evolution of the mixture concentration in the mushy zone can be expressed as:

$$\frac{\partial c_{\text{mix}}}{\partial t} = -f_\ell \bar{u}_\ell \cdot \nabla c_\ell \quad (2)$$

The evolution of  $c_{\text{mix}}$  can be analyzed from the flux of the interdendritic melt flow  $f_\ell \bar{u}_\ell$  and the gradient of the liquid concentration  $\nabla c_\ell$ . If both vectors  $f_\ell \bar{u}_\ell$  and  $\nabla c_\ell$  point in the similar directions (the angle between the two vectors is smaller than  $90^\circ$ ), negative segregation will occur ( $\partial c_{\text{mix}} / \partial t < 0$ ). As shown in Figure 5a-b, this mechanism acts in the upper corner region of the ingot. Both the melt flow and the liquid concentration gradient have almost the

same direction. In the other words, solute-poor melt replaces the solute-rich melt in this region, and thus, leads to a negative segregation. In the opposite situation, if both vectors  $f_s \bar{u}_s$  and  $\nabla c_s$  point in the opposite directions (the angle between the two vectors is larger than  $90^\circ$ ), positive segregation will occur ( $\partial c_{\text{mix}} / \partial t > 0$ ). As shown in Figure 5a-b, this mechanism acts in the lower corner region of the ingot. In the other words, the melt leaving the region has a relative lower concentration than the melt which will feed the region. Please notice that Eq. (2) only applies if solidification shrinkage can be ignored.

The positive macrosegregation in the ingot centre (Figure 4) is formed gradually during solidification. As mentioned above, the interdendritic melt has a higher concentration than the bulk melt. The interdendritic solute-enriched melt is brought out of the mushy zone by the flow current, causing  $c_{\text{mix}}$  in front of or slightly behind the columnar tip front to be enriched gradually. These positively enriched melts are not stationary, they move with the flow current, and finally meet in the casting centre and form a large positive segregation zone.

### Case 3: Sedimentation-induced macrosegregation

Here the same benchmark ingot (Figure 3) is simulated, but now with the assumption of globular equiaxed solidification. The purpose is to study the formation of macrosegregations by the mechanisms of grain sedimentation and sedimentation-induced convection during equiaxed solidification. The model assumptions and process conditions are summarized:

- Mould filling is ignored: solidification starts with an initial concentration Fe-0.34 wt.% C and an initial temperature of 1785 K;
- Two phases are considered: the melt and globular equiaxed grains. We suppose that there is no columnar phase appearing in the solidification process;
- The grain morphology is approximated as spheres;
- A three-parameter heterogeneous nucleation law is used:  $n_{\text{max}} = 1 \times 10^{11} \text{ m}^{-3}$ ,  $\Delta T_\sigma = 4 \text{ K}$ ,  $\Delta T_N = 10 \text{ K}$ ;
- Solidification shrinkage is not considered, a Boussinesq approximation is used to treat the buoyancy force for the grain sedimentation. Solid and liquid densities are  $\rho_l = 7027 \text{ kg}\cdot\text{m}^{-3}$  and  $\rho_s = 7321 \text{ kg}\cdot\text{m}^{-3}$ , respectively.
- Grains in the bulk melt can move freely up to a volume fraction of  $f_s^c = 0.637$ , the ‘‘packing limit’’;
- Constant heat transfer coefficients and constant mould and air temperatures are used (Figure 3);
- A 2D axis symmetric simulation is performed.

The dynamic evolution sequence of the equiaxed phase, including sedimentation and resulting macrosegregations is shown in Figure 6. At the initial stage, grains which nucleate in the upper regions and at the side walls sink downwards. The sinking grains drag the surrounding melt with them, and thus cause the melt to sink along the wall and rise in the casting centre. Two axis symmetric melt convection rolls develop in the melt. The relative velocity

$\bar{u}_e - \bar{u}_l$  always points downwards. The sinking grains lead to an accumulation of solid in the bottom region of the casting and cease to move when the local fraction of solid exceeds the packing limit. Events such as grain nucleation, grain growth and sedimentation continue until the late stage of solidification. The ‘hot spot’ in the casting is very close to the top surface. This is due to the overall melt convection and the small heat transfer coefficient at the top of the ingot.

The relative motion between the equiaxed grains and the melt results in the formation of macrosegregations. This mechanism can be analysed with (Appendix C):

$$\frac{\partial c_{\text{mix}}}{\partial t} = (c_l - c_s) \nabla \cdot (f_s \bar{u}_s). \quad (3)$$

In the case of  $c_l > c_s$ , a positive value of  $\nabla \cdot (f_s \bar{u}_s)$  would lead to a positive segregation. Here,  $\nabla \cdot (f_s \bar{u}_s)$  is the volumetric flux balance for the moving solid phase. It means that, when there is more solid phase leaving than entering the volume element,  $\nabla \cdot (f_s \bar{u}_s)$  gets positive, and thus a positive segregation forms. This mechanism is also schematically illustrated in Figure 7a, which corresponds to a situation where solute poor grains are replaced by the solute rich melt. The opposite is shown in Figure 7b. Now, more solid phase enter the volume element than it leave, and thus  $\nabla \cdot (f_s \bar{u}_s)$  gets negative and negative segregation forms. In the other words, the replacement of solute rich melt by the solute poor grains leads to negative segregation.

As shown in Figure 6, in the initial stage the solute-poor grains at the top corner regions sink and fresh melt is drawn into the corners, causing positive segregation, i.e. the mechanism shown in Figure 7a operates. At the bottom corners, the solute-poor grains settle and ‘squeeze’ the solute-enriched melt out of the corners, causing negative segregation, i.e. shown in Figure 7b. However, at the top corners the positive segregation zones are actually not stationary. They move downwards along the wall and then move slowly away from the wall towards the casting centre. This is due to the fact that the positive segregation zones are associated with fluid and thus may move with melt convection. As visible in Figure 6b-c, along the casting top surface the melt flows continuously into the corner and thus develops a local circulation current, causing a motion of the positive segregation region. The positive segregated area, as it moves, becomes wider and wider. The grains continue to grow, sink, and eventually leave the enriched melt behind. While sedimentation goes on, the bottom negative segregation zone becomes larger and larger as well. The grains pile-up slowly, creating a relatively large negative segregation zone at the bottom. Due to the coupling of melt flow and grain movement, the  $c_{\text{mix}}$  field is slightly modified in the last stages of solidification. However, the primary mechanism responsible for negative segregation at the bottom of the casting is due to mechanism as shown in Figure 7b.

#### Case 4: Macroseggregation in mixed columnar-equiaxed solidification

A more complex model for the mixed columnar-equiaxed solidification is used to simulate a similar benchmark ingot as that shown in Figure 3. Macroseggregation formation due to the combined thermosolutal convection, grain sedimentation, and sedimentation induced convection is investigated here. The model assumptions are summarized as follows:

- Mould filling is ignored, solidification starts with an initial concentration Fe-0.34 wt.% C and an initial temperature of 1785 K;
- Three phases are considered: the melt, globular equi-axed grains and columnar dendrite trunks;
- Morphologies are approximated by step-wise growing cylinders for columnar dendrite trunks and spheres for globular equi-axed grains;
- Columnar trunks grow from side and bottom walls, and the columnar tip front is explicitly tracked;
- A three-parameter heterogeneous nucleation law is used for the nucleation of the equi-axed grains:  $n_{\max} = 5 \times 10^9 \text{ m}^{-3}$ ,  $\Delta T_{\sigma} = 2 \text{ K}$ ,  $\Delta T_{\text{N}} = 5 \text{ K}$ . No fragmentation and grain attachment are currently considered;
- Shrinkage flow is ignored. The buoyancy force of the moving grains and the thermosolutal convection are accounted for by a Boussinesq approximation;
- The grains ahead of the columnar tip front can move if their volume fraction is below the "packing limit,"  $f_s^c = 0.637$ ;
- Hunt's blocking mechanism [14] is applied for predicting CET (columnar-to-equi-axed transition);
- Constant heat transfer coefficients and constant mould and air temperatures are used (Figure 3);
- A full 3D calculation is performed.

The solidification sequence including sedimentation of the globular equi-axed grains, the sedimentation-induced and thermosolutal buoyancy-driven melt convection are shown in Figure 8a. The solidification pattern agrees with the classical explanation of steel ingot solidification, summarized by Campbell [15]. The columnar dendrites grow from the mould wall and the columnar tip front moves inwards. The equi-axed grains nucleate near the mould walls and in the bulk melt. The columnar dendrites are stationary, whereas the equi-axed grains sink and settle in the base region of the ingot. The accumulation of such grains at the base of the ingot has a characteristic cone-shape. The sedimentation of grains and the melt convection influence the macroscopic solidification sequence and thus, the final phase distribution. More equi-axed grains will be found at the bottom and in the base region, while columnar solidification will be predominant in the upper part of the ingot.

As the columnar tip front is explicitly tracked, the simulation shows that the columnar tip fronts from both sides tend to meet in the casting centre. However, in the lower part of the casting the large amount of equi-axed grains stops the propagation of the columnar tip front. Its final position indicates the CET position. The CET separates the

areas where only equi-axed grains appear from the areas where both columnar dendrites and equi-axed grains coexist.

The predicted final macroseggregation distribution is shown in Figure 8b. From the simulation results it is obvious that the main mechanism for the cone-shaped negative segregation in the base region is grain sedimentation. The settling grains are poor in solute and thus their pile-up results in a negative segregation at the bottom of the ingot. A further contributing factor to the strength of this negative segregation comes from the flow divergence of the residual liquid through this zone at a late solidification stage. The positive segregation at the top region of the ingot is caused by the flow of the enriched melt in the bulk region. This kind of positive segregation coincides with classical experimental results [15]. It should be noted that channel segregations, which are frequently found in large steel ingots, are not predicted in such a reduced ingot.

#### Summary

The multiphase simulation results presented here shed light on a range of flow and sedimentation phenomena and their impact on the formation of macroseggregation. The main insights can be summarized as follows:

- Feeding flow-induced macroseggregations in a 1-D unidirectional solidification situation, as studied by Flemings et al. with their LSRE analytical equation [7-8], can be reproduced by the current multiphase approach.
- When solidification shrinkage is ignored, the formation of macroseggregations in the mushy zone due to interdendritic flow (e.g. thermosolutal buoyancy force driven flow) can be analyzed from the flux of the interdendritic melt flow  $f_i \bar{u}_i$  and the gradient of the interdendritic melt concentration,  $\nabla c_i$  (see Eq. (2)). If both  $f_i \bar{u}_i$  and  $\nabla c_i$  point in a similar direction, negative segregation forms; if both  $f_i \bar{u}_i$  and  $\nabla c_i$  point in opposite directions, positive segregation occurs.
- The sedimentation-induced macroseggregation can be analyzed from the flux balance of the moving solid phase  $\nabla \cdot (f_s \bar{u}_s)$  (see Eq. (3)). For an alloy with the solute partitioning coefficient  $k$  less than one, for example, if there is more solid phase leaving than entering the local volume element, positive segregation forms. Otherwise, if there is more solid phase entering than leaving the local volume element, negative segregation appears.

Finally, we would like to state that due to the considered model assumptions and simplifications, a quantitative comparison of the model predictions with industry processes is not recommended at this stage. Future work, however, will include the necessary refinements required to successfully create a multiphase model compatible with industrial castings.

## Appendices

### A. LSRE equation

Formulations of the Eulerian volume averaged mass and species conservations for a two-phase (liquid and columnar) solidification are as follows:

$$\frac{\partial}{\partial t}(f_s \rho_s) + \nabla \cdot (f_s \rho_s \bar{u}_s) = M_{fs}, \quad (\text{A-1})$$

$$\frac{\partial}{\partial t}(f_l \rho_l) + \nabla \cdot (f_l \rho_l \bar{u}_l) = -M_{fs}, \quad (\text{A-2})$$

$$\frac{\partial}{\partial t}(f_s \rho_s c_s) + \nabla \cdot (f_s \rho_s \bar{u}_s c_s) = \nabla \cdot (f_s \rho_s D_s \nabla c_s) + C_{fs}, \quad (\text{A-3})$$

$$\frac{\partial}{\partial t}(f_l \rho_l c_l) + \nabla \cdot (f_l \rho_l \bar{u}_l c_l) = \nabla \cdot (f_l \rho_l D_l \nabla c_l) - C_{fs}. \quad (\text{A-4})$$

As assumed in the Flemings' model [7-8]:

- The densities of both solid and liquid are constant. The solidification shrinkage coefficient is calculated as  $\beta = (\rho_s - \rho_l) / \rho_s$ ;
- Global species transport by diffusion is ignored:  $D_l = 0, D_s = 0$ ;
- In the interdendritic region,  $D_l$  is assumed to be infinite, and no back diffusion in the solid dendrite is considered. Species partitioning occurs at the liquid-solid interface:  $\partial(f_s \rho_s c_s) / \partial t = c_s^* \rho_s \partial f_s / \partial t$ , where  $c_s^* = k c_l$ .

The sum of Eq. (A-3) and Eq. (A-4) is,

$$-k c_l \rho_l \frac{\partial f_s}{\partial t} + \rho_l c_l \frac{\partial f_l}{\partial t} + \rho_l f_l \frac{\partial c_l}{\partial t} + \nabla \cdot (f_s \rho_s c_s \bar{u}_s) + \nabla \cdot (f_l \rho_l c_l \bar{u}_l) = 0. \quad (\text{A-5})$$

Substituting Eq. (A-1) and Eq. (A-2) into Eq. (A-5) gives

$$\frac{\partial c_l}{\partial t} + \frac{(1-k)c_l}{(1-\beta)f_l} \frac{\partial f_s}{\partial t} + \bar{u}_l \cdot \nabla c_l = 0. \quad (\text{A-6})$$

From the relationship  $\dot{T} = -\bar{v}_T \cdot \nabla T$ , where  $\dot{T}$  is the local heating/cooling rate and  $\bar{v}_T$  is the moving speed of the isotherm, we have

$$\bar{u}_l \cdot \nabla c_l = -\frac{\bar{u}_l}{\bar{v}_T} \frac{\partial c_l}{\partial t}. \quad (\text{A-7})$$

Substituting Eq. (A-7) into Eq. (A-6), we get the LSRE equation

$$\frac{\partial f_l}{\partial c_l} = -\frac{(1-\beta)}{(1-k)} \left( 1 - \frac{\bar{u}_l}{\bar{v}_T} \right) \frac{f_l}{c_l} = 0. \quad (\text{A-8})$$

### B. Shrinkage-free segregation

With the assumptions:

- No solidification shrinkage, i.e. the densities of both liquid and solid phases are constant and equal;
- Global species transport by diffusion is ignored  $D_l = 0, D_s = 0$ ;
- The solid dendrite trunks are stationary,  $\bar{u}_s = 0$ .

The sum of the volume averaged species conservations, Eq. (A-3) and Eq. (A-4), gives

$$\frac{\partial c_{\text{mix}}}{\partial t} + \nabla \cdot (f_l c_l \bar{u}_l) = 0. \quad (\text{B-1})$$

Considering the mass conservation equations Eq. (A-1) and Eq. (A-2), one gets  $\nabla \cdot (f_l \bar{u}_l) = 0$ , and so

$$\frac{\partial c_{\text{mix}}}{\partial t} = -f_l \bar{u}_l \cdot \nabla c_l. \quad (\text{B-2})$$

The point product of two vectors is positive when both vectors point into similar directions (the angle between them is smaller than  $90^\circ$ ). So, with similar directions of the melt flux,  $f_l \bar{u}_l$ , and the liquid concentration gradient,  $\nabla c_l$ , a reduction of the mixture concentration  $c_{\text{mix}}$  will be the consequence.

### C. Sedimentation-induced segregation

With the assumptions:

- No solidification shrinkage;
- Global species transport by diffusion is ignored  $D_l = 0, D_s = 0$ ;
- The volume averaged concentration gradient in the melt and grains are ignored:  $\nabla c_l = 0, \nabla c_s = 0$ .

The sum of the volume averaged species conservations, Eq. (A-3) and Eq. (A-4), gives

$$\frac{\partial c_{\text{mix}}}{\partial t} + c_l \nabla \cdot (f_l \bar{u}_l) + c_s \nabla \cdot (f_s \bar{u}_s) = 0. \quad (\text{C-1})$$

According to the mass conservation equations, Eq. (A-1) and Eq. (A-2), it yields that  $\nabla \cdot (f_s \bar{u}_s) = -\nabla \cdot (f_l \bar{u}_l)$ . Therefore Eq. (C-1) gives

$$\frac{\partial c_{\text{mix}}}{\partial t} = (c_l - c_s) \nabla \cdot (f_s \bar{u}_s), \quad (\text{C-2})$$

where  $\nabla \cdot (f_s \bar{u}_s)$  is the divergence of the solid phase flux. From Eq. (C-2) it follows, that if more solid phase leaving than entering the volume element,  $\nabla \cdot (f_s \bar{u}_s)$  gets positive, and so mixture concentration  $c_{\text{mix}}$  increases.

## Nomenclature

$C_{fs}$ ( $\text{kg} \cdot \text{m}^{-3} \cdot \text{s}^{-1}$ )	species transfer from liquid to solid;
$c_0$ (-)	initial concentration;
$c_{\text{mix}}$ (-)	mixture concentration;
$c_l$ (-)	liquid concentration;
$c_l^*$ (-)	liquid equilibrium concentration;
$c_s : c_c / c_e$ (-)	concentration of different solid phases;
$c_s^*$ (-)	solid equilibrium concentration;
$D_l$ ( $\text{m}^2 \cdot \text{s}^{-1}$ )	diffusion coefficient in liquid phase;
$D_s$ ( $\text{m}^2 \cdot \text{s}^{-1}$ )	diffusion coefficient in solid phase;
$f_l$ (-)	volume fraction of melt;
$f_s : f_c / f_e$ (-)	volume fraction of different solid phases;
$f_s^c$ (-)	packing limit of equiaxed phase;
$\bar{g}$ ( $\text{m} \cdot \text{s}^{-2}$ )	gravity;

$k$ (-)	solute partitioning coefficient;
$M_{ls}$ ( $\text{kg}\cdot\text{m}^{-3}\cdot\text{s}^{-1}$ )	mass transfer rate from liquid to solid;
$n_{\text{max}}$ ( $\text{m}^{-3}$ )	maximum available nucleation sites;
$T$ (K)	temperature;
$T_0$ (K)	initial temperature;
$T_E$ (K)	eutectic temperature;
$T_w$ (K)	mould wall temperature;
$\Delta T_N$ (K)	undercooling for maximum grain production rate;
$\Delta T_\sigma$ (K)	Gaussian distribution width of nucleation law;
$t$ (s)	time;
$\bar{u}_l$ ( $\text{m}\cdot\text{s}^{-1}$ )	velocity of melt;
$\bar{u}_s : \bar{u}_e$ ( $\text{m}\cdot\text{s}^{-1}$ )	velocity of solid (equiaxed) phase;
$\bar{v}_T$ ( $\text{m}\cdot\text{s}^{-1}$ )	moving speed of isotherm;
$x_{T_E}$ (m)	position of eutectic isotherm;
$x_{\text{tip}}$ (m)	position of columnar tip;
$x_{T_L}$ (m)	position of liquidus isotherm;
$\beta$ (-)	solidification shrinkage coefficient;
$\beta_c$ (-)	solute expansion coefficient;

$\beta_T$ (-)	thermal expansion coefficient;
$\rho_l, \rho_s$ ( $\text{kg}\cdot\text{m}^{-3}$ )	densities of liquid and solid phases.

References

- [1] M.C. Flemings: ISIJ Intern., 40 (2000), 833.
- [2] C. Beckermann: Int. Mater. Rev., 47 (2002), No. 5, 243.
- [3] G. Lesoult: Mater. Sci. Eng. A, 413-414 (2005), 19.
- [4] K. Schwerdtfeger: Metallurgie des Stranggießens, Verlag Stahleisen mbH, Düsseldorf, 1992.
- [5] I. Ohnaka: Metals Handbook, Castings, 15 (1998), USA: ASM International, 136.
- [6] M. Wu, A. Ludwig: Adv. Eng. Mater., 7 (2005), No. 9, 846.
- [7] M.C. Flemings, G.E. Nereo: Trans. TMS-AIME, 239 (1967), 1449.
- [8] M.C. Flemings, G.E. Nereo: Trans. TMS-AIME, 242 (1968), 50.
- [9] H. Kato, J.R. Cahoon: Metall. Trans. A, 16A (1985), 579.
- [10] M. Wu, A. Ludwig: Metall. Mater. Trans. A, 37A (2006), 1613.
- [11] A. Ludwig, M. Wu: Mater. Sci. Eng. A, 413-414 (2005), 109.
- [12] M. Wu, A. Ludwig: Metall. Mater. Trans. A, 38A (2007), 1465.
- [13] V.R. Voller, S. Sundarraj: Int. J. Heat Mass Transfer, 38 (1995), No. 6, 1009.
- [14] J. D. Hunt: Mater. Sci. Eng., 65 (1984), 75.
- [15] J. Campbell: Castings, Butterworth Heinemann Ltd, Oxford, 1991.

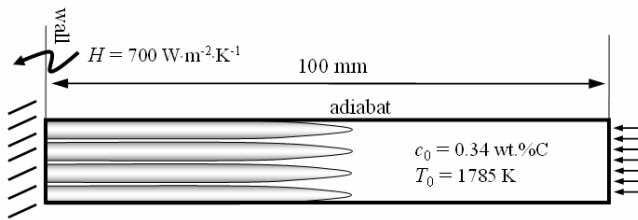
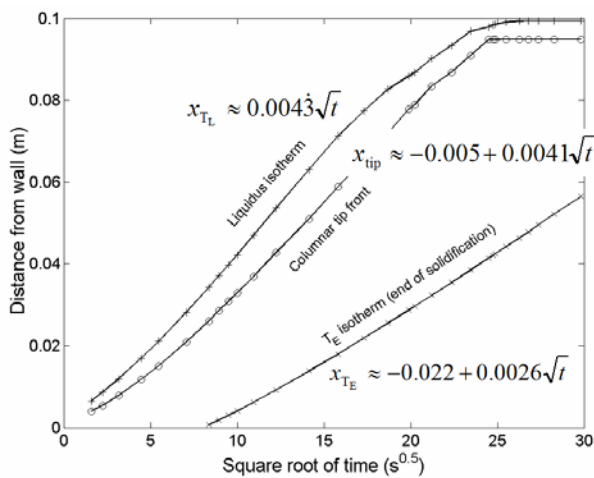
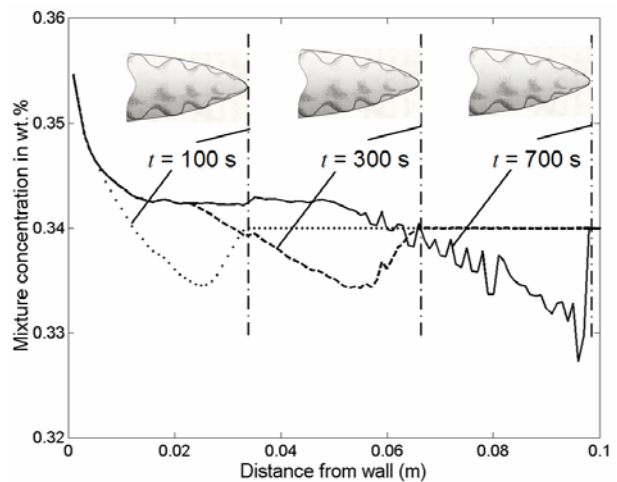


Figure 1. Configuration of the benchmark of a 1D unidirectional solidification.



(a)



(b)

Figure 2. Feeding induced macrosegregation in a 1D columnar solidifying configuration. a) Calculated position of the liquidus isotherm, the columnar tip front and the eutectic isotherm as function of the square root of time; b) calculated macrosegregation profiles in terms of  $c_{\text{mix}}$  (in wt.%C) predicted at three different instants in time.

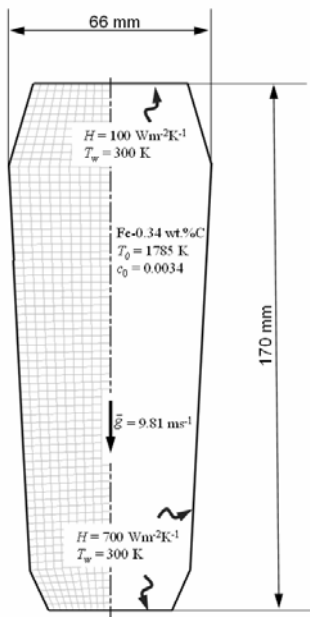


Figure 3. Configuration of a reduced steel ingot.

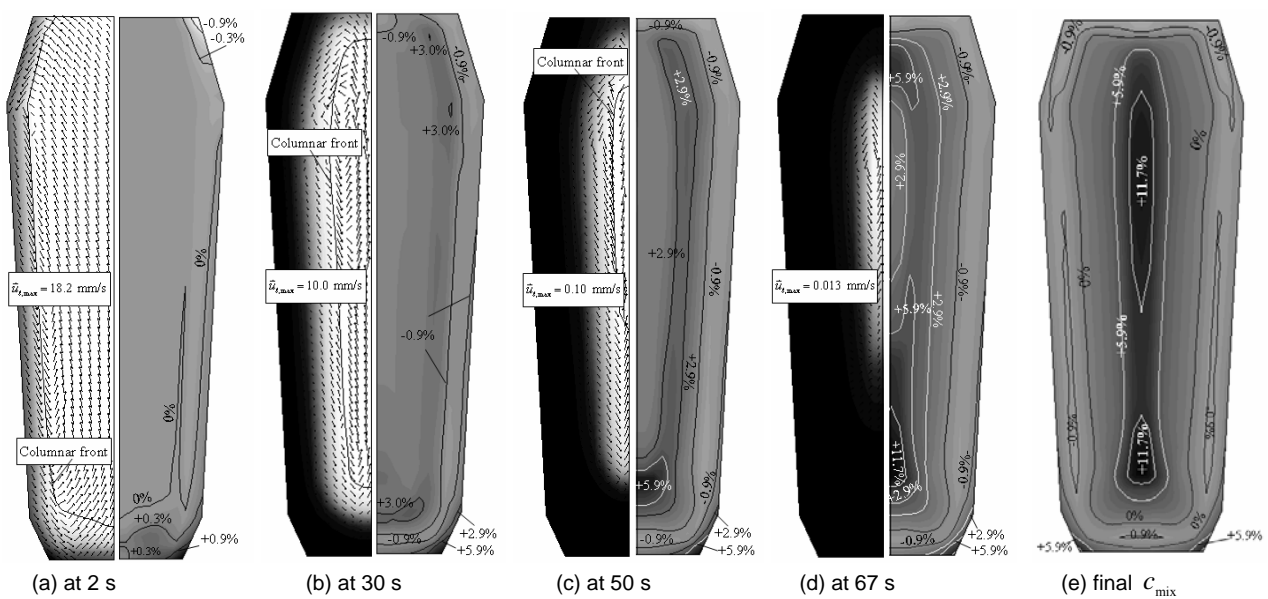
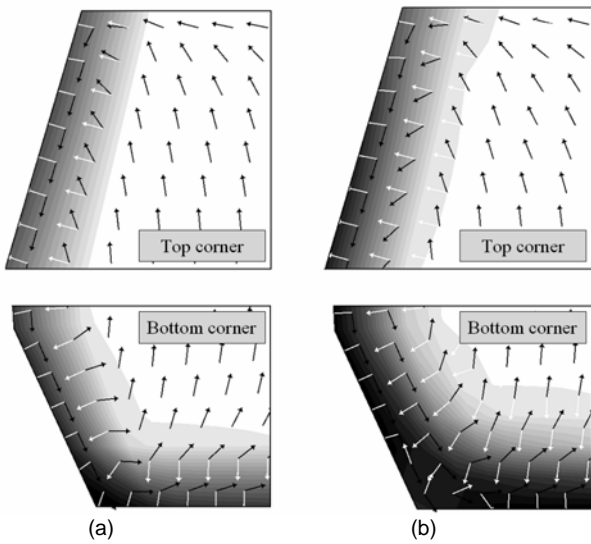
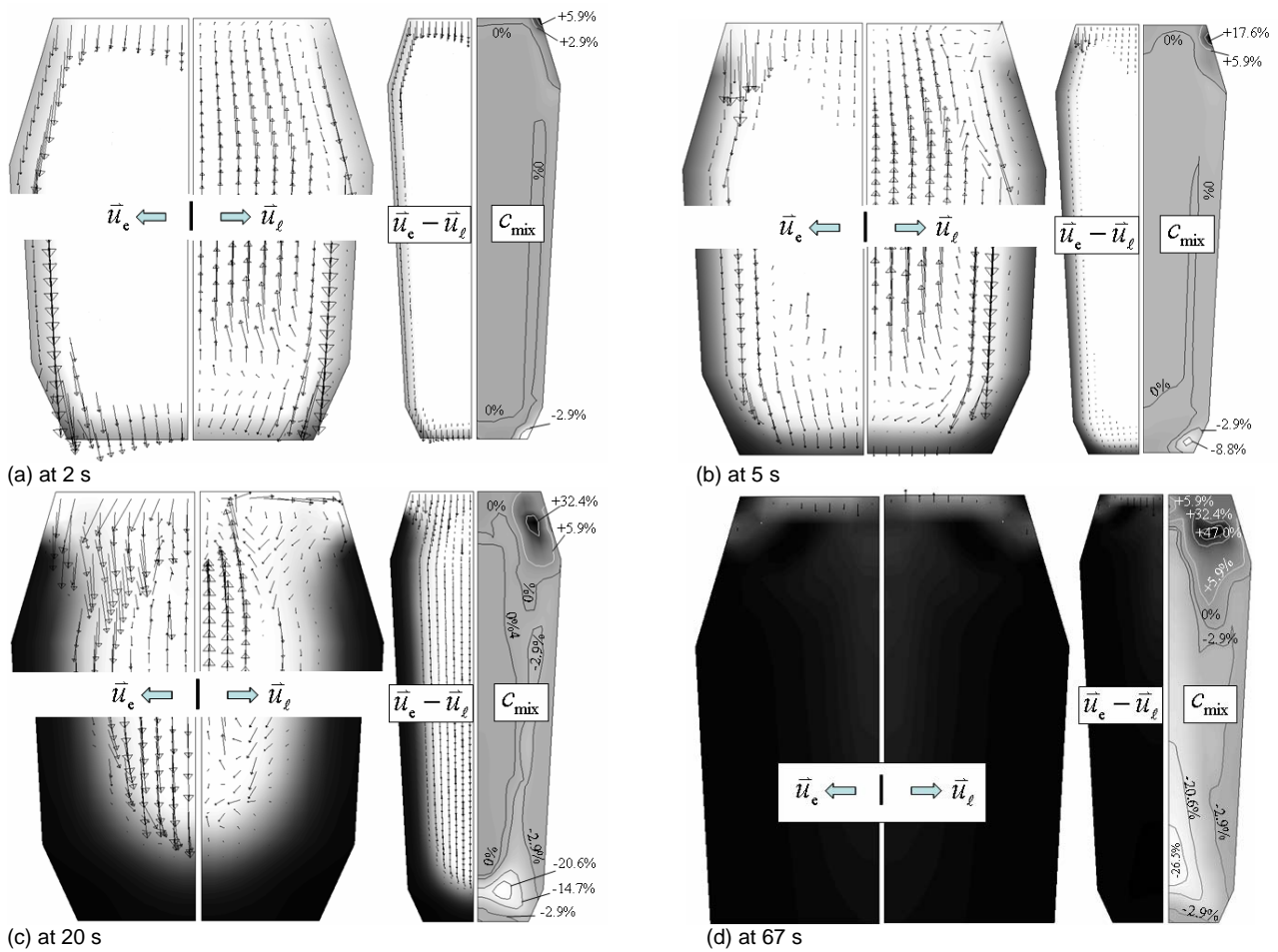


Figure 4. Predicted solidification sequence and macrosegregation formation induced by thermosolutal convection in the reduced steel ingot. The left half of a)-d) shows the volume fraction evolution of the columnar phase in gray scale with the columnar tip position indicated with a solid line. The right half of the series shows the evolution of the macrosegregation, gray-scaled according to positive and negative segregation. The macrosegregation index in % is calculated as  $100 \times (c_{\text{mix}} - c_0) / c_0$ . The predicted final macrosegregation pattern is shown in figure e).



**Figure 5.** Analysis of the formation of macrosegregation in the initial stage namely a) at 0.5 s, and b) at 1.0 s. Here only corner regions are investigated. The liquid concentration  $c_l$  is shown by the gray scale with dark for the highest concentration and light for the lowest concentration. The black arrows indicate the direction of the melt flow  $\vec{u}_l$ , whereas the white arrows indicate the direction of the liquid concentration gradient  $-\nabla c_l$ .



**Figure 6.** Predicted solidification sequence and formation of macrosegregation induced by grain sedimentation. The volume fraction of equiaxed grains  $f_e$  is shown in gray-scale (light for  $f_e = 0$  and dark for  $f_e = 1$ ), and overlaid with the equiaxed velocity  $\vec{u}_e$ , melt velocity  $\vec{u}_l$ , and the relative velocity  $\vec{u}_e - \vec{u}_l$ . The distribution of  $C_{mix}$  is also shown in gray-scale. The macrosegregation index in % is calculated as  $100 \times (c_{mix} - c_0) / c_0$ . The final macrosegregation pattern is almost identical to the one at 67 s.

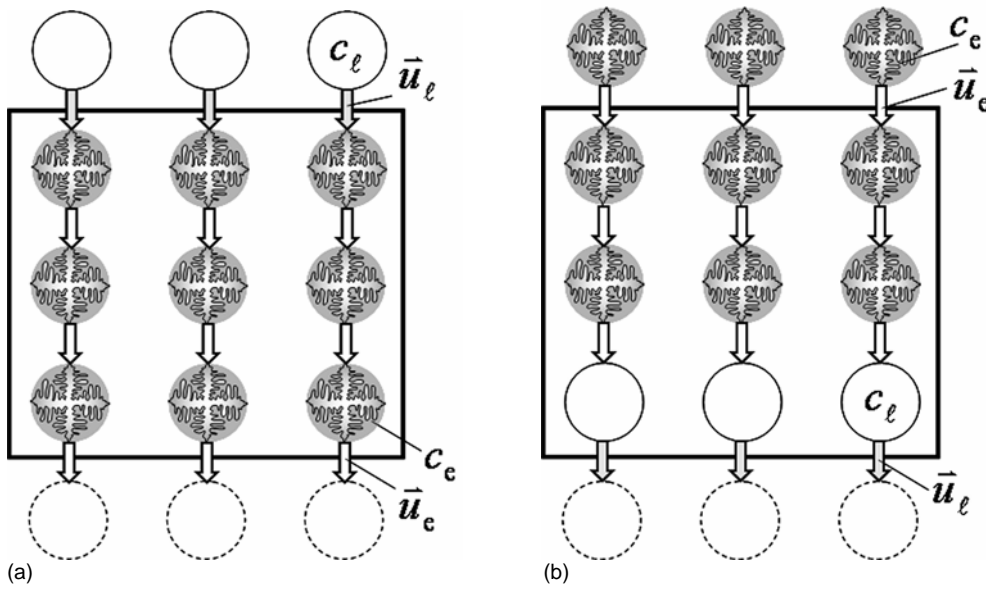


**Figure 7.** Macrosegregation formation mechanisms ( $k < 1$ ) by grain sedimentation, a) positive segregation formed by replacing the solute poor grains with solute rich melt; b) negative segregation formed by replacing the solute rich melt with solute poor grains.

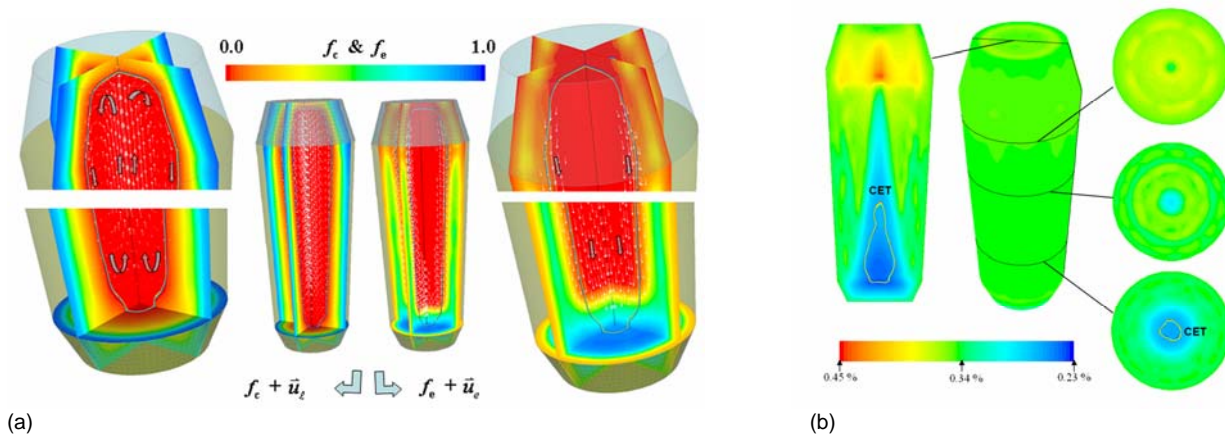


**Figure 8.** a) Simulated solidification sequence (at 20 s) of the steel ingot.  $f_c$  and  $f_e$  are shown in colour in two vertical and one horizontal sections, the velocity fields  $\vec{u}_l$  and  $\vec{u}_e$  are shown as vectors. The columnar tip front position is also shown. b) Predicted mix concentration  $c_{mix}$  in the steel ingot, scaled from 0.23 wt.% C to 0.45 wt.% C. The area of 100 % equiaxed macrostructure is surrounded by the CET line.